ADVANCED FUNCTIONAL MATERIALS
www.afm-journal.de

Multi-Faceted Binder Enhancement via Slurry-Applicable Thiol-Ene Click Chemistry for Low-Pressure-Operable All-Solid-State Batteries

*Young Joon Park, Kyu Tae Kim, Seunggoo Jun, Jong Seok Kim, Jaehyun Yoon, Cheol Bak, Yong Min Lee, Dong Hyeon Kim, Ji Young Kim, and Yoon Seok Jung**

Ensuring low-pressure operability is imperative in the practical deployment of all-solid-state batteries (ASSBs) with sulfide solid electrolytes, highlighting the pivotal roles of functional binders. Herein, slurry-applicable thiol-ene click reaction-derived modifications of styrene-butadiene rubber (SBR) binders are introduced to enhance the electrochemo-mechanical stabilities of composite cathodes under low operating pressures. Two key modifications are realized: the grafting of carboxylate functional groups to improve the adhesion and cross-linking to enhance the modulus and elasticity. A key insight gained is that cross-linking is considerably more critical in improving the low-pressure performance than adhesion enhancement. Electrochemical evaluations using single-crystalline $LiNi_{0.8}Co_{0.1}Mn_{0.1}O_2$|$Li_6PS_5Cl$|(Li-In) half-cells at 0.3 MPa indicate that $LiNi_{0.8}Co_{0.1}Mn_{0.1}O_2$ electrodes with the cross-linked binder exhibit superior electrochemical performances, including higher initial discharge capacities and improved initial Coulombic efficiencies and capacity retentions compared to those of the unmodified-SBR-based electrodes (163 vs. 133 mA h g^{-1}, 68% vs. 73%, and 67% vs. 75% at the 100th cycle, respectively). Comprehensive analyses, including operando electrochemical pressiometry, reveal that cross-linking effectively maintains the electrode integrity, thereby stabilizing the interfacial resistance during cycling. These findings offer critical design guidelines for practical, high-performance ASSB systems.

1. Introduction

All-solid-state batteries (ASSBs) with sulfide solid electrolytes (SEs), such as Li argyrodites (e.g., Li_6PS_5Cl (LPSCl)), exhibit considerable potential for use in improving energy density and safety.[1–11] With multiple battery manufacturers and automotive companies actively advancing their commercialization, the transition to practical deployment is increasingly tangible.[12,13] Alongside their high ionic conductivities, this advancement is largely attributed to the mechanical deformabilities of sulfide SEs, which facilitate the scalable fabrication of large-format ASSBs via cold or warm pressing.[14–17] However, despite their deformabilities, sulfide SEs still form limited ionic contacts via pressing, leaving substantial voids,[18] and the complex spatial distribution of SE particles within the composite cathode further exacerbates the tortuosity.[12,19] Incorporating polymeric binders into commercially relevant sheet-type electrodes introduces an additional obstacle by further disrupting the interfacial ionic contacts.[17,20–22] These challenges stand in stark contrast to conventional lithium-ion battery electrodes, where liquid electrolytes readily permeate the porous structures, ensuring complete 2D ionic contacts.

From a binder perspective, Li^+-conductive binders can alleviate the binder-induced disruption of interfacial Li^+ transport. Our group developed several slurry-fabricable Li^+-conductive binders, including gel polymer electrolyte-type binders based on solvate

Y. J. Park, Dr. K. T. Kim, Dr. S. Jun, J. S. Kim, J. Yoon, Prof. Y. M. Lee, Prof. Y. S. Jung
Department of Chemical and Biomolecular Engineering
Yonsei University
Seoul 03722, Republic of Korea
E-mail: yoonsjung@yonsei.ac.kr

The ORCID identification number(s) for the author(s) of this article can be found under https://doi.org/10.1002/adfm.202516017

DOI: 10.1002/adfm.202516017

Y. J. Park, Prof. Y. S. Jung
Department of Battery Conflation Engineering
Yonsei University
Seoul 03722, Republic of Korea

C. Bak, Prof. Y. M. Lee
Department of Energy Science and Engineering
DGIST
Daegu 42988, Republic of Korea

Dr. D. H. Kim, J. Y. Kim
LG Energy Solution, Ltd.
LG Science Park
Seoul 07796, Republic of Korea

ionic liquids, i.e., lithium bis(trifluoromethanesulfonyl)imide (LiTFSI) complexes with triethylene glycol dimethyl ether,[21,23] and solid polymer electrolyte-type binders, such as LiTFSI-nitrile butadiene rubber, which were formulated using slurry-processing solvents, such as benzyl acetate or cosolvents of dibromomethane and hexyl butyrate.[24] Alternatively, binders with enhanced adhesion properties can reduce the required binder contents of electrodes, thereby minimizing the interfacial Li^+ disruption.[25] For example, Lee et al. enhanced the levels of adhesion within cathodes by grafting carboxylic acid groups onto styrene-butadiene block copolymers within binders,[26] whereas Li et al. introduced an ethylene-methyl acrylate copolymer, enabling the modulation of the polar and nonpolar functional groups to fabricate thin, flexible SE membranes with high ionic conductivities.[27]

In ASSBs, the initial formation of intimate ionic contacts is crucial, and their sustained integrity is equally critical, as even minor volume changes of the active materials during repeated charge–discharge cycling can significantly disrupt these contacts.[17,28–31] This challenge is particularly pronounced under low external operating pressures, typically constrained to a few megapascals in practical applications,[17,28] whereas conventional ASSB studies primarily rely on pellet-type cells without binders operating under exceedingly high pressures reaching hundreds of megapascals.[11,17,28] Three major strategies have been explored to enable ASSB operation at low pressures.[28,32–35] The first approach aims to minimize the volume changes of the cathode active material (CAM), thereby mitigating the structural stress within the composite electrode. Gao et al. reported that reducing the charging cut-off voltage from 4.4 to 4.2 V (vs. Li/Li^+) effectively limited CAM expansion, and operating at 80 °C facilitated Li^+ transport at 2 MPa.[32] The second strategy focuses on reinforcing the CAM-SE interface to maintain stable ionic conduction despite CAM expansion. Kim et al. reported a capacity retention of 93.7% at 0.1C after 100 cycles by uniformly coating $LiNi_{0.5}Co_{0.2}Mn_{0.3}O_2$ with a 30 nm layer of LPSCl, demonstrating a stable performance under the minimal operating pressures realizable in a coin cell.[33] Finally, the development of advanced binders with enhanced mechanical and interfacial functionalities has emerged as a key enabler of low-pressure operability.[36–39] Our group introduced a 3D cross-linked network into a butadiene rubber binder via vulcanization, effectively suppressing particle slippage at the cathode-SE interlayer and enhancing the electrochemical performance at 2 MPa.[28] However, the precise roles of binders within cathode composites, where the electrochemo-mechanical degradation is most pronounced, remain insufficiently elucidated.[40]

Herein, to enhance the low-pressure performances of ASSBs, we modified styrene-butadiene rubber (SBR) binders via the thiol-ene click reaction, leveraging its high reaction yields, rapid kinetics, and wide applicability, and the abundance of C=C bonds within the polymer structures:[41–43] i) grafting polar functional groups and ii) cross-linking. First, introducing carboxylic acid groups enhanced the adhesive strengths of electrodes, as verified by surface and interfacial cutting analysis system (SAICAS) and peel-off tests. Second, SBR was interwoven using trimethylolpropane tris(3-mercaptopropionate) (TMPT) as a cross-linker, imparting strain resistance against the external localized stress and preserving the structural integrity of the electrode. The resulting cross-linked binders exhibited improved mechanical properties, including increased Young's moduli and elasticities. Notably, thiol-ene click-based cross-linking was seamlessly integrated into the slurry process in situ, effectively bypassing gelation and polarity mismatch problems. Performance evaluation of single-crystalline $LiNi_{0.8}Co_{0.1}Mn_{0.1}O_2$ (NCM)|LPSCl|(Li-In) cells at 30 °C and 0.3 MPa confirmed the superior performances of the cross-linked binders compared to those of pristine or grafted SBR.

2. Results and Discussion

The two modifications realized via the thiol-ene click reaction at the electrode level–grafting and cross-linking of the SBR binders–are shown in **Figure 1**. SBR is a linear polymer featuring benzene rings along its main chain and two distinct types of C=C bonds: trans and vinyl. When thiol (–SH)-containing reactants are introduced, the thiol-ene click reaction proceeds via covalent bonding between the thiol and vinyl groups (–CH=CH_2), which is initiated by a thermal radical, such as azobisisobutyronitrile (AIBN). 3-Mercaptopropionic acid (3MPA), which contains carboxylic acid groups, is introduced to enhance adhesion, whereas TMPT is utilized as the cross-linker to reinforce the mechanical properties. The three thiol groups of TMPT form covalent bonds with the allyl groups of SBR, resulting in a cross-linked 3D network structure (Figure 1a).

Notably, these thiol-ene click reactions proceed in situ during wet-slurry electrode fabrication, as shown in Figure 1b. Nonpolar or low-polarity solvents, such as xylene, are commonly utilized in the wet-slurry processing of sulfide SEs to prevent side reactions with the SEs.[20,44,45] However, when grafted SBR (denoted g-SBR) is separately synthesized and redissolved in *p*-xylene, its increased polarity leads to poor solubility due to polarity mismatch (Figure S1, Supporting Information). Similarly, separately prepared cross-linked SBR (denoted X-SBR) swells but does not dissolve, hindering the formation of a homogeneous binder solution (Figure S1, Supporting Information). To address these challenges, cathode slurries were prepared using the binder precursors, incorporating NCM, LPSCl, SBR, AIBN, and 3MPA or TMPT, followed by casting and drying. The click reaction was then induced via heating to ensure uniform reaction progression and homogeneous binder integration.[46] This in situ preparation approach enables greater flexibility in both the type and amount of grafted functional groups.

Pristine SBR, g-SBR, and X-SBR were characterized using Fourier transform infrared (FTIR) spectroscopy, SAICAS and peel-off tests, and galvanostatic charge–discharge studies of ASSB cells, as shown in **Figure 2**. The FTIR spectra identify the presence of the characteristic functional groups, confirming their successful incorporation into each modified sample (Figure 2a). The three polymers exhibit the fundamental SBR structure, including aromatic C–H (698 cm^{-1}) and trans (968 cm^{-1}), and vinyl (910 cm^{-1}) C=C bonds.[47] Notably, as the click reaction proceeds, the thiol groups preferentially react with the vinyl C=C bonds instead of the trans configuration, leading to reduced vinyl/trans ratios within g-SBR (0.914) and X-SBR (0.854) compared to that within SBR (1.327). This selectivity is consistent with previous studies.[48] Additionally, the successful grafting of carboxyl groups into g-SBR is confirmed by the peak

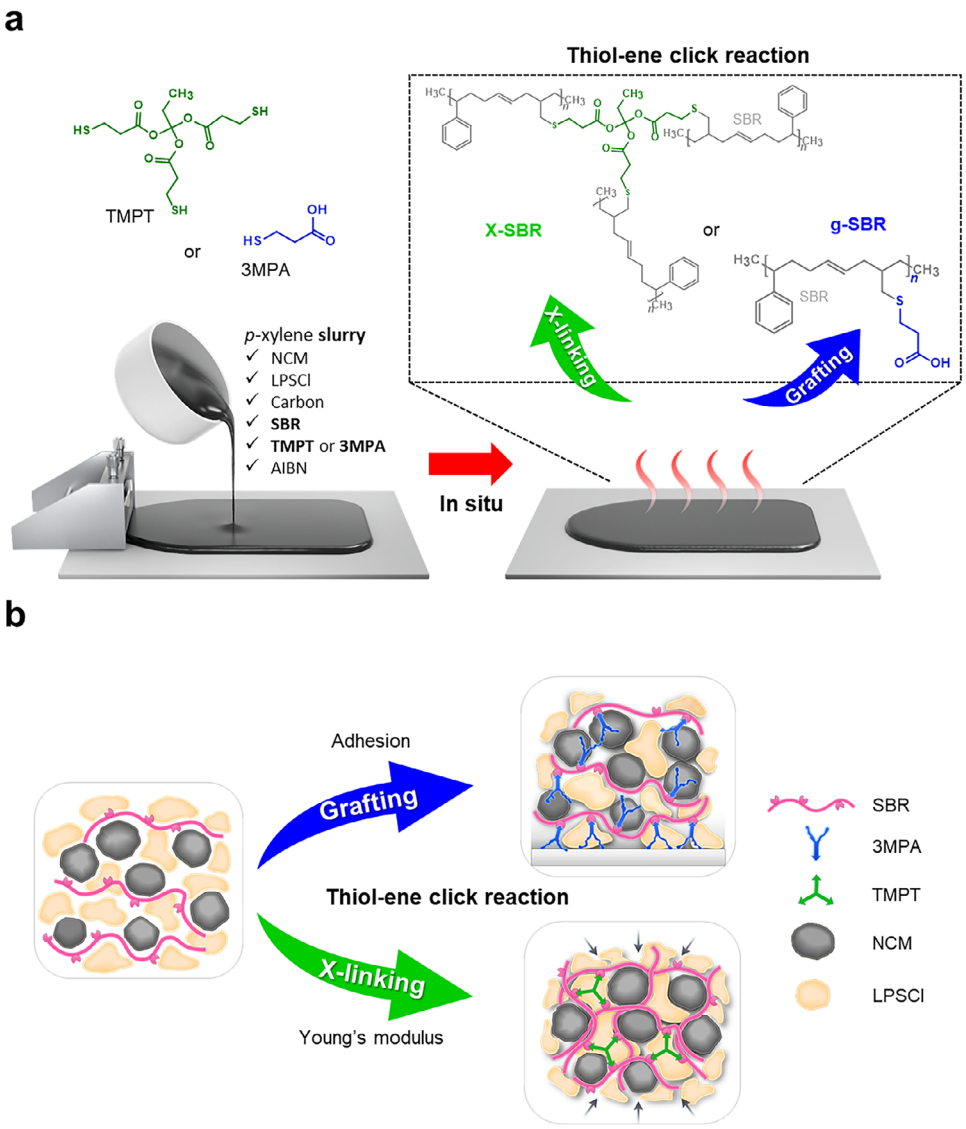

Figure 1. Two synthetic routes toward the SBR binders via the thiol-ene click reaction. a) Reaction mechanisms of grafting and cross-linking via reactions between SBR and thiol-functionalized molecules. b) Schematic illustrating the role of each modified binder. Conducting carbon additives are omitted in (b) for clarity of visualization.

at 1714 cm^{-1}. The formation of cross-linked structures within X-SBR is indicated by the presence of C═O and C–O peaks at 1740 and 1180 cm^{-1}, respectively, further validating the success of the click reaction.[49]

The effects of these modifications on adhesion at the electrode level were evaluated via two complementary analyses: SAICAS and peel-off tests. In electrode structures, the interfacial interactions – particle-particle and particle-current collector – are critical. As shown in Figure 2b, SAICAS analysis was performed to assess the adhesion strengths at various electrode depths from the electrode surface to the Al current collector/cathode interface. g-SBR exhibits the highest adhesion forces at all depths compared to those of SBR and X-SBR (e.g., 227, 389, and 234 N m^{-1} for SBR, g-SBR, and X-SBR, respectively, at their interfaces). The enhanced adhesion of g-SBR is likely due to hydrogen-bonding interactions facilitated by the grafted carboxylic acid moieties.[26] This result is further corroborated by the results of the peel-off test results, where g-SBR displays significantly stronger adhesion (≈150 N m^{-1}) than that of SBR (≈6 N m^{-1}) or X-SBR (≈8 N m^{-1}, Figure 2c). In addition, we examined the uniformity of binder distribution by analyzing adhesion–time profiles in SAICAS measurements at different depths (Figure S2, Supporting Information).[51,52] X-SBR electrodes showed the smallest adhesion fluctuations both within and across depths compared with SBR and g-SBR electrodes, confirming that binder distribution in X-SBR electrodes remains more uniform and stable during the in situ reaction.

NCM||(Li-In) all-solid-state half-cells were evaluated at 0.2C, 0.3 MPa, and 30 °C between 3.0 and 4.4 V (vs. Li/Li^+) to assess the influence of the improved adhesion on the electrochemical performance at a low operating pressure, with the initial

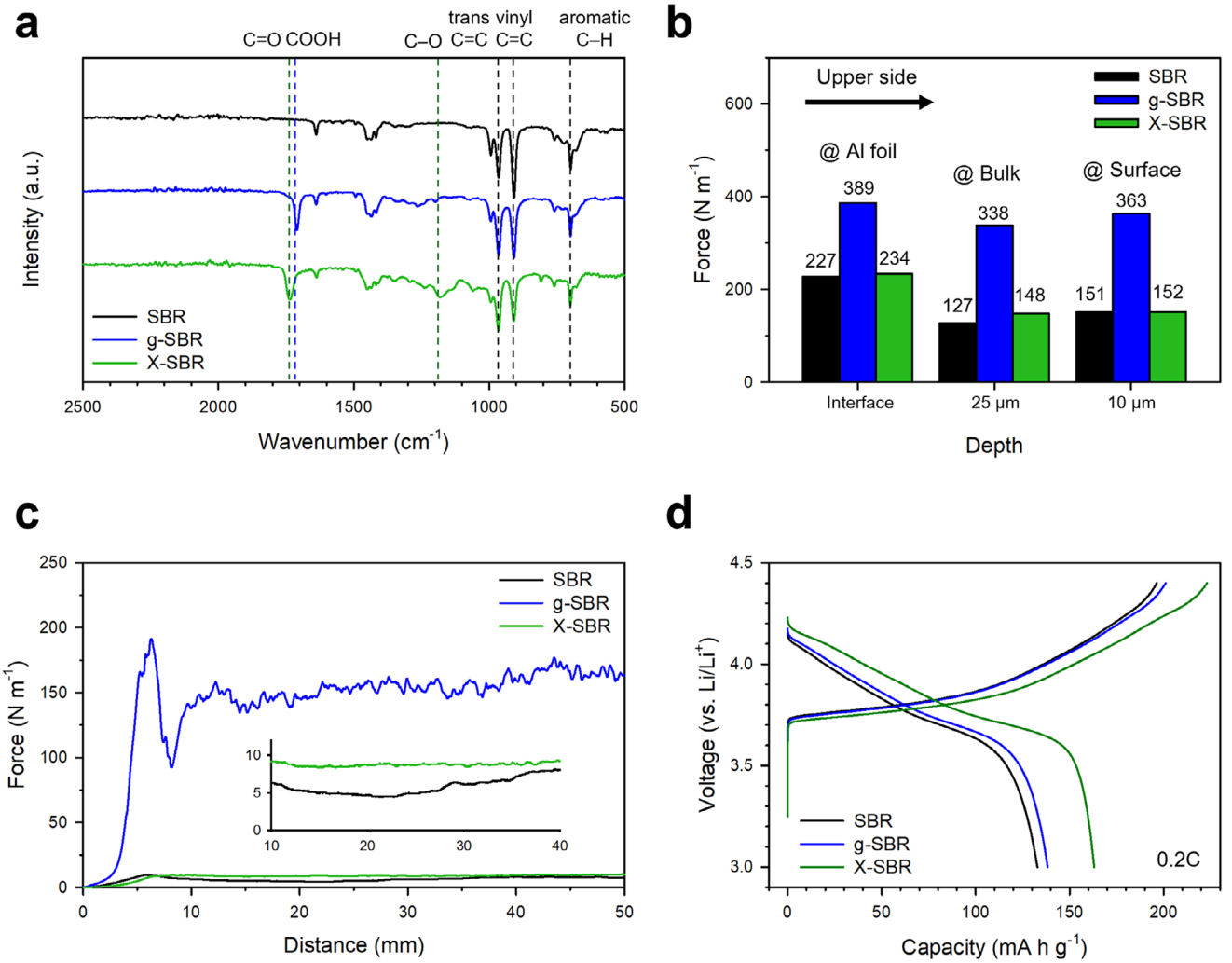

Figure 2. Material characterization and electrochemical performances of the electrodes with SBR, g-SBR, and X-SBR. a) FTIR spectra and results of the b) SAICAS and c) peel-off test results. d) First-cycle charge–discharge voltage profiles of NCM||(Li-In) cells at 0.2C, 30 °C, and 0.3 MPa.

charge–discharge voltage profiles shown in Figure 2d. The conditions of low operating pressure (0.3 MPa) and high cut-off voltage (4.4 V) were chosen to accentuate detrimental chemo-mechanical effects. Unexpectedly, the electrodes with g-SBR exhibit only marginal increases in their initial discharge capacities from 133 to 138 mA h g^{-1} compared to those of the electrodes with SBR. By contrast, X-SBR delivers a significantly higher capacity of 163 mA h g^{-1}, despite its considerably lower adhesion strength. This result suggests that factors beyond adhesion play more dominant roles in the low-pressure operation of ASSBs, underscoring the necessity of further investigation. The mechanisms underlying the enhanced performance of X-SBR shall be explored in detail in the following section.

We systematically adjusted the TMPT content and conducted FTIR spectroscopy and swelling, tensile, and nanoindentation studies to investigate the performance and corresponding mechanical properties of X-SBR as functions of cross-linking density, and the results are shown in **Figure 3**. The corresponding X-SBR samples are labeled such that the number following "X" represents the mass ratio of TMPT relative to SBR. The results of X-SBR shown in Figure 2 correspond to those of X10.

An increase in the TMPT content leads to a higher degree of click reaction, as indicated by a decrease in the intensity of the vinyl C═C peak. Conversely, the intensities of the peaks corresponding to the C═O and C–O bonds of the cross-linked structure increase (Figure 3a). Additionally, in situ cross-linking within the electrode slurries was confirmed (Figure S3, Supporting Information). The electrodes were rinsed with deionized water and ethanol to enhance the polymer signal and eliminate interference due to the SEs. Consistent with prior findings,[53] the intensity of the peak representing the vinyl C═C of SBR is comparable to or higher than that of the peak representing trans C═C. By contrast, the intensity of the peak representing the vinyl C═C of X10, where the click reaction occurs, is lower than that of the peak representing trans C═C. Swelling studies were performed to further quantify the extent of cross-link formation (Figure 3b). Expectedly, the degree of swelling decreases as the TMPT concentration increases from 6 to 14 wt.%, indicating a

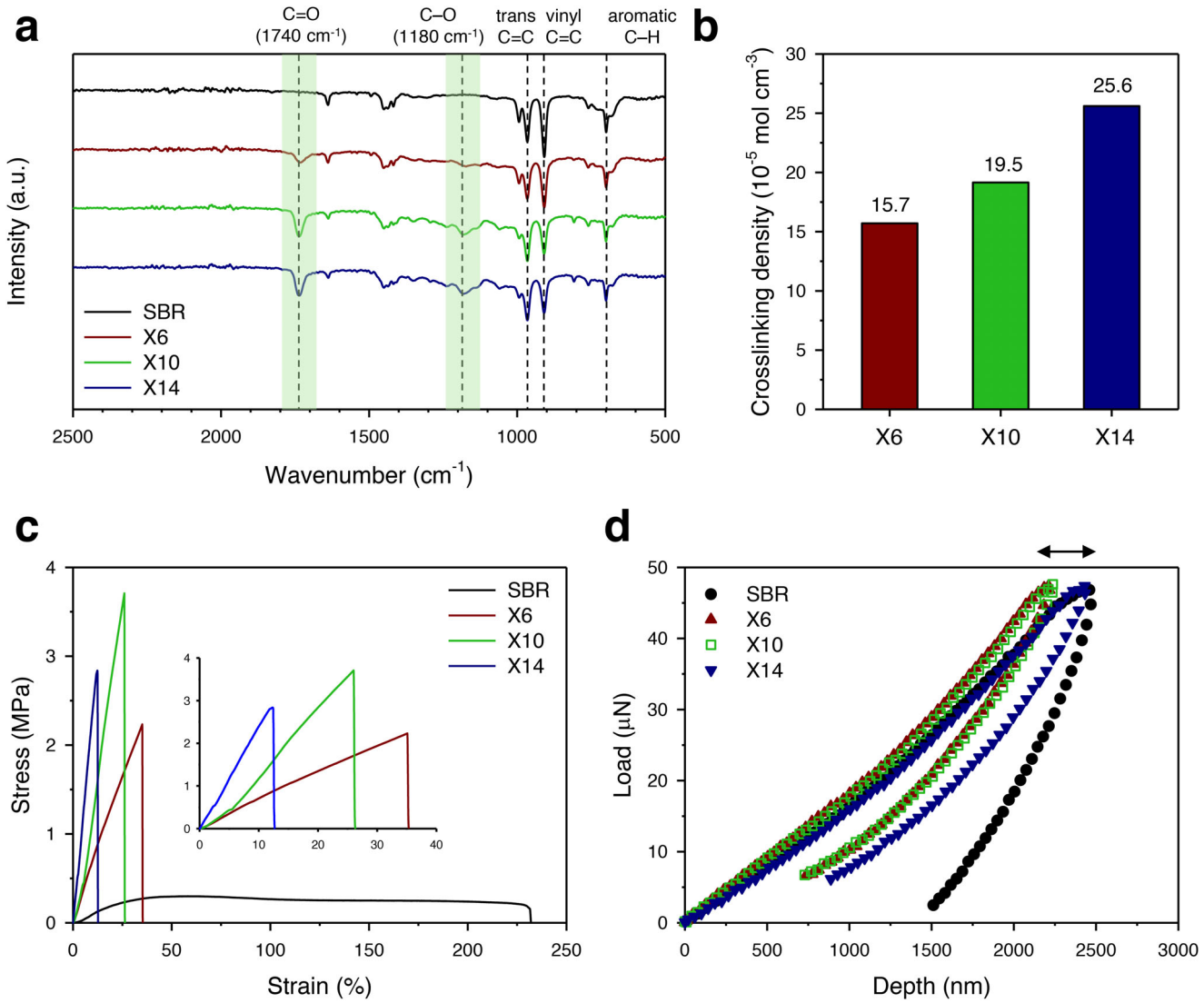

Figure 3. Characterization of SBR and X-SBR (X6, X10, and X14) with different cross-linker mass ratios. a) FTIR spectra and the results of the b) swelling, c) tensile, and d) nanoindentation studies.

higher cross-linking density (e.g., (15.7, 19.5, and 25.6) × 10^{-5} mol cm^{-3} for X6, X10, and X14, respectively).[28,54]

The mechanical properties of the X-SBR samples were evaluated by measuring their Young's moduli using a universal testing machine and performing nanoindentation tests, with the results shown in Figure 3c,d, respectively. The stress–strain curve of pristine SBR reveals a typical rubber-like behavior, with no failure observed, even at high strains of up to 200% (Figure 3c), whereas the X-SBR samples fail at significantly lower strains of <50%. Notably, a higher cross-linking density results in an increased Young's modulus (Table S1, Supporting Information), which is consistent with previous findings.[55,56] For example, the Young's modulus of SBR is 0.78 MPa, whereas that of X10 reaches 14.3 MPa – an enhancement of ≈18-fold. These results suggest that the cross-linked binder is more effective in resisting local stresses generated during charge–discharge cycling within the composite electrode, thereby minimizing strain accumulation and reducing particle detachment. Nanoindentation analysis provided further insights into the mechanical properties of X-SBR at the nanoscale (Figure 3d). Under an identical load of 50 μN, cross-linked X6 and X10 exhibit shallower indentation depths compared to those of SBR, indicating their increased resistance to deformation. Additionally, upon removing the external forces, X10 displays a higher elastic recovery than that of SBR (66.3% compared to 38.2%), reflecting its enhanced capacity to return to its original shape. These results collectively confirm that X-SBR exhibits a superior mechanical robustness and elasticity under compressive and tensile loads at the micro- and macro-scales. Such properties should contribute to maintaining the electrode integrity during the low-pressure operation of an ASSB cell.

Building on the outperformance of the electrodes with X-SBR over those with pristine SBR, as validated by the screening study shown in Figure 2d, further electrochemical studies were conducted using NCM||(Li-In) cells at 30 °C and 0.3 MPa.

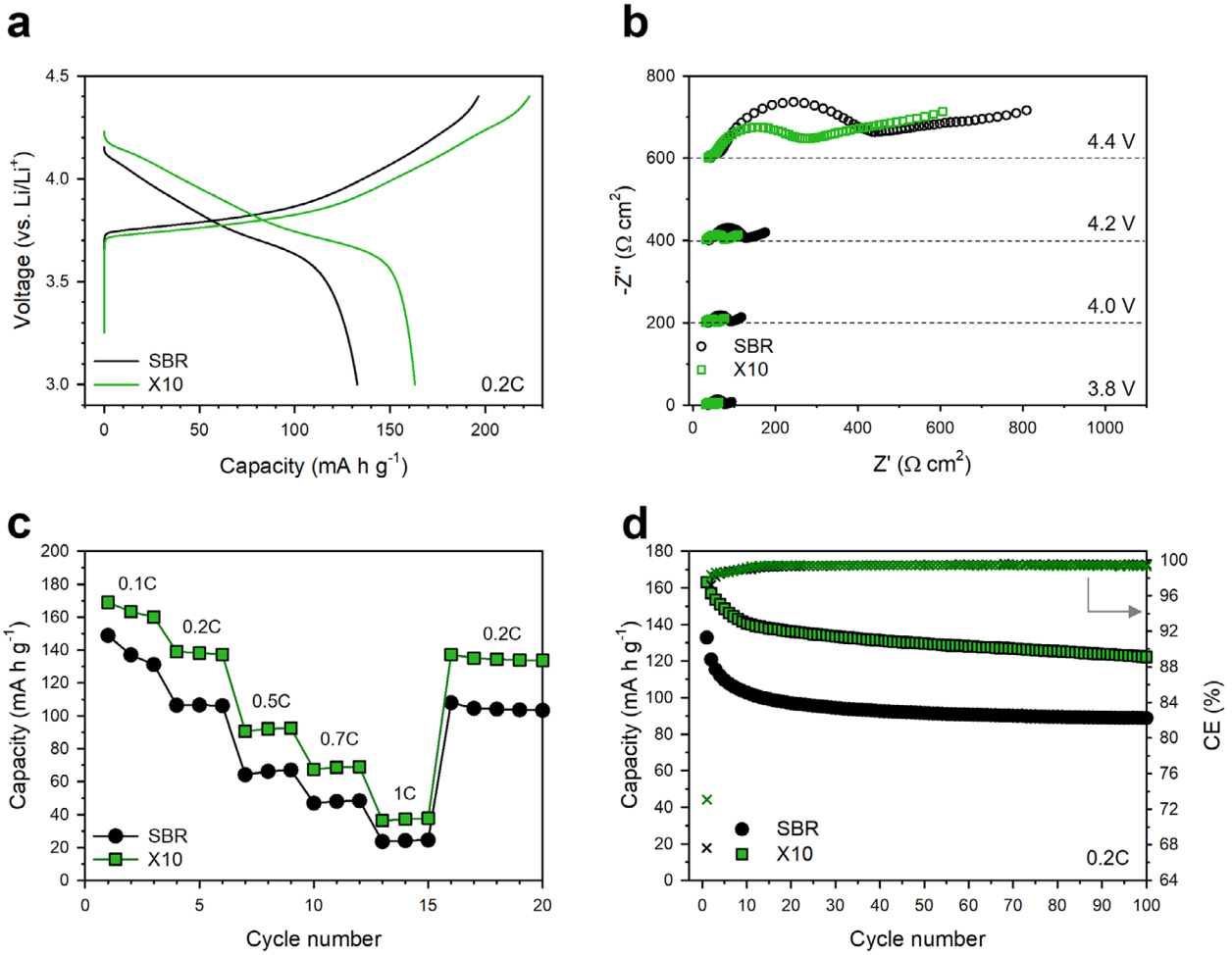

Figure 4. Comparative electrochemical characterization of the NCM electrodes with SBR and X10 in NCM||(Li-In) cells at 30 °C and 0.3 MPa. a) First-cycle charge–discharge voltage profiles at 0.2C, b) Nyquist plots at various cut-off voltages during charging, c) rate capabilities, and d) cycling performances at 0.2C.

With increasing cross-linking density (X6 → X10 → X14), the electrochemical performance followed a consistent trend: cycle retention after 100 cycles (66.8 → 72.7 → 75.0 → 71.0%) and ICE (67.6 → 70.8 → 73.1 → 71.6%) improved up to X10 (Figure S4, Supporting Information). Notably, all electrodes with cross-linked binders (X6, X10, and X14) exhibit superior performances compared to that of the electrode with pristine SBR, with the X10 electrodes delivering the optimal performance. Based on the results of X-ray diffraction (XRD), electrochemical impedance spectroscopy (EIS), and cyclic voltammetry (CV), as shown in Figures S5 and Table S2 (Supporting Information), the extent of the in situ click reaction displays no adverse effects on the electrochemical properties of LPSCl (see the details in the Supporting Note S1, Supporting Information). However, top-view scanning electron microscopy (SEM) images of the electrodes reveal that excessive cross-linking densities lead to particle agglomeration (Figure S6, Supporting Information), likely explaining the optimal performances of the X10 electrodes. Accordingly, the comparative results obtained using the X10 and SBR electrodes are shown in **Figure 4**. Along with the substantially higher discharge capacity of the X10 electrode compared to that of the SBR electrode (163 against 133 mA h g^{-1}), the X10 electrode displays a correspondingly substantially lower overpotential (Figure 4a). Notably, the difference in overpotential increases toward the end of charging, where detachments within the electrodes due to the volume changes of the CAMs become more significant. A similar trend is observed in the direct current internal resistances (DCIRs, Figure S7, Supporting Information), with the X10 electrode exhibiting a lower internal resistance of 92.2 Ω compared to that of the SBR electrode of 124.5 Ω.

In situ EIS was performed at different voltages during the initial charge to further investigate the evolution of the interfacial resistance, and the corresponding Nyquist plots are shown in Figure 4b. The equivalent circuit model and fitted values are shown in Figure S8 and Table S3 (Supporting Information), respectively. The Nyquist plots display characteristic flattened semicircles followed by Warburg tails, corresponding to the interfacial resistances and Li^+ diffusion within the CAMs, respectively.[57] Across all voltages, the X10 electrode consistently exhibits a lower interfacial resistance than that of the SBR electrode. Analyzing the fitted values reveals negligible differences in the R_1 values, corresponding

to the bulk resistances of the LPSCl separating layers – between the SBR and X10 electrodes across different states of charge (SOCs). Similarly, the R_2 values of the two electrodes, representing the grain boundary resistances of the LPSCl layers, remain comparable and exhibit similar SOC-dependent increases, which are attributed to side reactions. However, a pronounced increase in R_3, which is associated with the interfacial charge transfer resistance, is observed as charging proceeds. This increase is partially attributed to volume changes of NCM during Li^+ extraction, leading to interfacial delamination between NCM and LPSCl.[58] Notably, this increase differs between the two electrodes. The R_3 of SBR increases from 79.8 to 759.8 Ω, whereas that of X10 increases from only 28.6 to 293.2 Ω. This may be attributed to the superior mechanical properties of X10, where its higher modulus enables more effective strain mitigation under the same applied stress, thereby effectively maintaining the interfacial stability.

Consistently, as shown in Figure 4d, the X10 electrode displays a superior capacity retention of 75.0% compared to that of the SBR electrode (66.8%). Furthermore, the capacity retention and initial Coulombic efficiency increase with a higher degree of cross-linking until X10 (Figure S9, Supporting Information), followed by a decline at X14, confirming the beneficial role of cross-linking. The reduced performance of the X14 electrode is attributed to agglomeration (Figure S6, Supporting Information). Notably, the performance differences between the pristine and cross-linked SBR electrodes are negligible under a high operating pressure of 70 MPa (Figure S10, Supporting Information), reinforcing the significance of enhanced mechanical properties in improving the performance under a low operating pressure.

Operando electrochemical pressiometry (OEP) and in situ XRD of the SBR and X10 electrodes were conducted to gain deeper insight into the electrochemo-mechanical behaviors influenced by the cross-linking of the SBR binders, and the corresponding results are shown in **Figure 5**. In OEP, zero-strain $Li_4Ti_5O_{12}$ (LTO) was used as the anode,[59] ensuring that the pressure variations within the cells originated solely from the cathodes (Figure 5a). The operability of the LTO electrode in an LTO||(Li-In) half-cell was validated, as shown in Figure S11 (Supporting Information). Figure 5b shows the initial charge–discharge voltage profiles of the NCM||LTO cells at 0.2C, 30 °C, and 3 MPa, along with their corresponding variations in pressure ($\Delta P = P - P_{initial}$). The X10 electrode exhibits a larger overpotential and correspondingly higher capacity compared to those of the SBR electrode. Notably, the ΔP profiles reveal that the X10 electrode exhibits a smaller ΔP variation than that of the SBR electrode, except at the end of charging (Region 2). As shown in Figure 5c, the decrease in ΔP during charging is attributed to the volume contraction caused by Li^+ extraction from NCM, leading to a reduction in the cathode thickness.[29,60] Given the similar levels of Li^+ extraction, this result suggests that the cross-linked binder within the X10 electrode effectively suppresses the volumetric changes of the composite cathode, resulting in smaller ΔP variations and reduced interfacial delamination in Region 1. Additionally, the X10 electrode exhibits a higher ΔP recovery at the end of discharge (Region 3), which is consistent with the high elasticity of X-SBR observed in Figure 3c,d, and the reversible charge–discharge behavior.

However, the magnitude of ΔP of the X10 electrode is larger than that of the SBR electrode at the end of charging (Region 2), which remains unresolved. In situ XRD was conducted to compare the absolute volumetric changes of the NCM unit cells to clarify this (Figure 5d–g). The SOC variations of the SBR and X10 electrodes were tracked using the position of the (101) peak (Figure 5e,f), which reflects changes in the lattice parameters along the a and c-axes.[61,62] During charging, a consistent shift toward a higher 2θ corresponds to lattice contraction. Notably, the X10 electrode exhibits a larger $\Delta(2\theta)$ shift than that of the SBR electrode (Figure 5g), indicating higher Li^+ extraction due to its lower overpotential at the end of charging,[63,64] which suggests that the X10 electrode displays a higher SOC. The more negative ΔP (i.e., larger magnitude) of the X10 electrode at the end of charging (Region 2) in Figure 5b, despite the cross-linking-induced suppression of the volumetric shrinkage of the electrode composite, may be attributed to the more severe lattice contraction of NCM at a higher SOC. Furthermore, the X10 electrode exhibits a higher retention of the position of the (101) peak at the end of discharge, indicating its improved reaction reversibility compared to that of the SBR electrode.

Cross-sectional SEM images of the SBR and X10 electrodes were compared before and after charging to 4.4 V (vs. Li/Li^+) at the 100th cycle to assess the capacity of the binder to maintain the electrode integrity and suppress particle delamination (Figure 5h–l). In their pristine states, both electrodes exhibit intimate contacts between their particles, with negligible voids (Figure 5h,j), but the SBR electrode displays interparticle delamination accompanied by voids or cracks after the 100th charge, as highlighted by the red circles (Figure 5i). By contrast, although the X10 electrode also develops several cracks after charging, they are notably fewer than those within the SBR electrode (Figure 5k). Quantitative analysis using box plots further substantiates this trend (Figure 5l). Collectively, the results of OEP, in situ XRD, and cross-sectional SEM confirm that the mechanically reinforced X-SBR effectively suppresses delamination within the composite electrode, which arises from the volume changes of NCM during charge–discharge cycling. When compared with recent studies on low-pressure operability (Table S4, Supporting Information), our results are competitive in terms of both pressure range and the use of sheet-type electrodes.

Beyond the thiol-ene click-derived binder modifications demonstrated thus far, deliberate combinations of functional groups could enable additional functionalities. For instance, concurrent incorporation of –COOH and $–NH_2$ groups imparts self-healing ability, which can alleviate mechanical damage and facilitate crack recovery during cycling, as shown in Supporting Note S2 and Figures S12 and S13 (Supporting Information).[40,49] Further studies may also explore alternative cross-linkers with flexible linkages or polar moieties to better balance mechanical robustness and interfacial integrity.[65]

3. Conclusion

In summary, we demonstrated slurry-applicable thiol-ene click reaction-derived modifications of SBR binders that enhance the electrochemo-mechanical stabilities of the composite cathodes of ASSBs, particularly under low operating pressures. Two mod-

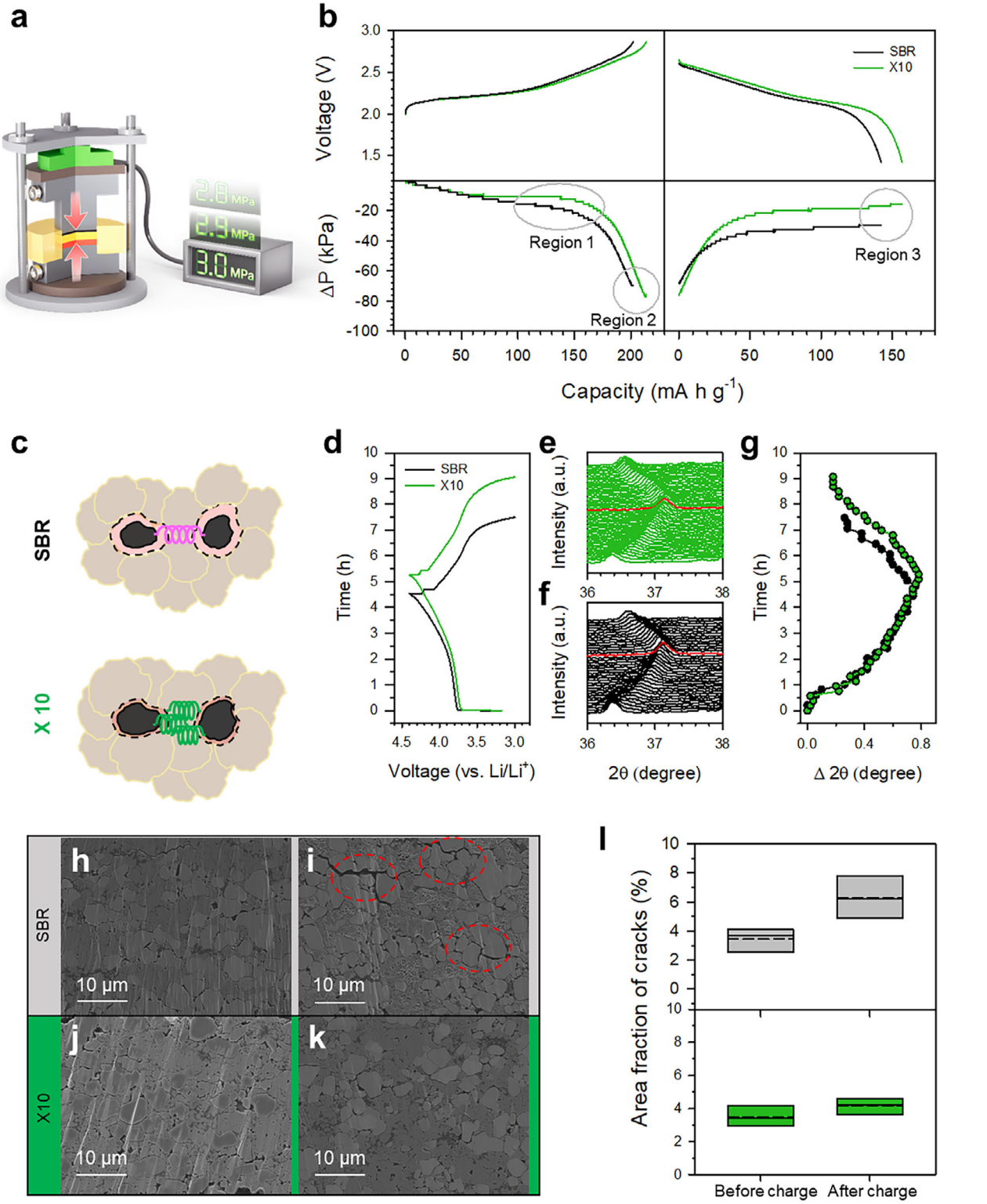

Figure 5. In situ or ex situ characterization of NCM electrodes with SBR or X10 at 0.2C, 30 °C, and 3 MPa. a) Schematic of the OEP measurement set-up and b) first-cycle charge–discharge voltage profiles of NCM||(LTO) cells with corresponding pressure changes. c) Schematic of the mechanisms corresponding to Region 1 in (b). d) First-cycle charge–discharge voltage profiles of NCM||(Li-In) cells during in situ XRD measurements. e,f) Corresponding in situ XRD reflections showing the evolution of the (101) reflection of NCM for X10 (e) and SBR electrodes (f). g) Associated changes in peak position, $\Delta(2\theta)$. h–k) Cross-sectional SEM images of SBR (h,i) and X10 electrodes (j,k) before cycling (h,j) and after charging to 4.4 V (vs Li/Li^+) at 100th cycles (i,k). l) Corresponding box plots of each area fraction of the voids, the median and mean values are represented by solid and dotted horizontal lines, respectively.

ifications were introduced: the grafting of carboxylate functional groups using 3MPA and cross-linking using TMPT. The former significantly improved the adhesion properties, as confirmed via SAICAS and peel-off tests. Critically, the latter was considerably more effective in improving the low-pressure operability of an ASSB, underscoring the distinct roles of the modulus and elasticity in reinforcing the mechanical integrity of the electrode. The NCM electrodes with the optimal X-SBR binder (X10) in NCM||(Li-In) half-cells exhibited initial discharge capacities of 163 mA h g^{-1} at 0.2C, 30 °C, and 0.3 MPa, along with capacity retentions of 75% after 100 cycles. In stark contrast, using electrodes with unmodified SBR resulted in initial discharge capacities and capacity retentions of 133 mA h g^{-1} and 67%, respectively. Complementary analyses using EIS, OEP, in situ XRD, and ex situ SEM revealed that cross-linking effectively preserved the electrode integrity by suppressing interparticle delamination and crack formation, thereby mitigating the accumulation of interfacial resistance caused by strain-induced degradation. The proposed in situ cross-linking strategy offers a potentially scalable route for use in enhancing binder functionality without compromising the electrochemical properties, paving the way for more robust and commercially viable ASSB technologies. Building on this foundation, further advances, such as self-healing capabilities, represent promising directions for future exploration.

4. Experimental Section

Preparation of Materials: SBR (LG Chem) was used as received, and thiol-ene-clicked binders were prepared via the reaction between SBR and 3MPA (99%, Sigma–Aldrich) or TMPT (95%, Sigma–Aldrich), wherein AIBN (99%, Daejung Chemicals & Metals) was used as a thermal initiator. After SBR and AIBN were dissolved in *p*-xylene (anhydrous, 99%, Sigma–Aldrich), 3MPA was added to form g-SBR with an SBR/3MPA/AIBN mass ratio of 100:18:10. In preparing X-SBR, TMPT was added in an SBR/TMPT/AIBN mass ratio of 100/x/10 (x = 6, 10, or 14). The resulting mixture was stirred for 5 min and then dried for 1 h at ambient pressure, followed by drying for 12 h under vacuum at 80 °C. For self-healing incorporation, cysteamine (95%, Sigma–Aldrich) was added in an equimolar ratio with 3MPA, and the overall content of grafted functional groups was fixed at 10 mol% of the binder. LPSCl was prepared via ball-milling and subsequent heating under an Ar atmosphere. A stoichiometric mixture of Li_2S (99.9%, Alfa Aesar), P_2S_5 (99%, Sigma–Aldrich), and LiCl (99.99%, Sigma–Aldrich) was ball-milled at 600 rpm for 10 h in a ZrO_2 vial with ZrO_2 balls using a Pulverisette 7PL (Fritsch). The mixture was then heated at 550 °C for 5 h under an Ar atmosphere. $LiNbO_3$-coated NCM (LG Chem) powders were used.

Electrode Fabrication: Wet slurries comprising NCM, LPSCl, Super C65 (Imerys Graphite & Carbon), and the binder precursors were prepared to yield the target compositions using *p*-xylene with a mass ratio of 75.0:22.5:1.0:1.5. The slurries were then cast onto carbon-coated Al using the doctor-blade method, followed by two-step drying: 1 h at ambient pressure, and then 12 h under vacuum at 80 °C. The electrodes for use in the SAICAS and peel-off tests, and top-view SEM measurements were prepared with NCM/binder compositions of 95:5 by mass to eliminate the effects of atmospheric reactions on the SEs and clearly observe the morphological changes. The LTO electrodes were fabricated by mixing LTO, LPSCl, and Super C in a mass ratio of 10.0:10.0:0.1.

Material Characterizations: FTIR spectroscopy was conducted using an ALPHA II (Bruker) in the range 4000–400 cm^{-1}, using 24 scans and a resolution of 4 cm^{-1} for each spectrum. The SAICAS was used to measure the adhesive strength of each layer of the composite electrode using a boron nitride microblade with a width and rake, and clearance angles of 1 mm, 20°, and 10°, respectively. The microblade moved vertically and horizontally at 0.2 and 2.0 μm s^{-1}, respectively, to cut the composite electrodes until the target depths were attained. After cutting the composite electrode at the target depth, the microblade moved only in the horizontal direction at 2.0 μm s^{-1} to cut the composite electrode and measure the horizontal force. The measured horizontal force was converted to the adhesive strength of each layer by dividing the corresponding force by the width of the blade. Tensile and 180° peel-off tests were performed using a multi-axis microtexture analyzer (TXA Texture Analyzer) at a speed of 0.5 mm s^{-1}. Polymer films of 1 × 4 cm were used in the tensile studies. In the peel-off test, tapes were uniformly attached to the electrodes using a 2 kg hand roller. Details of the cross-linking density measurements are described in the Supporting Information. Nanoindentation studies were conducted under a controlled load with a maximum force of 50 μN using a TI 950 (Bruker). The polymer films used in the nanoindentation studies were prepared on glass slides with a thickness of ≈20 μm. SEM was performed using an AURIGA scanning electron microscope (Carl Zeiss). The specimens were stored and transported using an airtight shuttle system to prevent exposure to ambient air. The samples used in cross-sectional SEM were prepared via cold-polishing at 6 kV for 6 h, followed by milling at 1.5 kV for 1 h with an Ar ion beam at −50 °C using an IB-19510CP (JEOL). Powder XRD was conducted using a MiniFlex600 diffractometer (Rigaku) with Cu Kα radiation (λ = 1.5406 Å). Powder XRD cells containing hermetically sealed SE samples with Be windows were mounted on the XRD diffractometer and measured at 40 kV and 15 mA. In situ XRD cells were charged and discharged between 3.0 and 4.4 V (vs. Li/Li^+) by applying a constant current of 0.05C at room temperature under an applied pressure of ≈1 MPa. The in situ XRD data were continuously recorded in the 2θ range 34°–40° at a step width of 0.02°. The in situ EIS cells were charged and discharged between 3.0 and 4.4 V (vs. Li/Li^+) at 0.2C and 30 °C, and the data were continuously recorded in the range 3.8–4.4 V at a step width of 0.2 V.

Electrochemical Characterization: The Li^+ conductivities were measured using the alternating-current impedance method and Li^+-blocking Ti|SE|Ti symmetric cells. Cold-pressed pellets with diameters of 6 mm were prepared at 370 MPa. The EIS data were recorded at an amplitude of 10 mV in the frequency range 10 mHz–7 MHz using a VMP3 (BioLogic). As a counter/reference electrode, Li-In (nominal composition of $Li_{0.5}In$) powder was prepared by mixing Li (Arcadium Lithium) and In (99%, Sigma–Aldrich) powders. ASSB cell assemblies were fabricated using poly(aryl-ether-ether-ketone) molds with diameters of 13 mm, with two Ti rods as the current collectors. First, 150 mg of LPSCl powder was pelletized to serve as the SE layer. Li-In (40 mg cm^{-2}) and the as-prepared NCM electrode (10 mg cm^{-2}) were then placed on each side of the SE layer. Finally, the assembled cell was pressed at 370 MPa. All NCM||(Li-In) cells were cycled between 3.0 and 4.4 V (vs. Li/Li^+) at 30 °C. (SE-C)||(Li-In) cells were fabricated for use in CV. An SE and Super C65 mixture with a mass ratio of 8:2 was used as the working electrode. The LPSCl layer served as the separating SE layer, whereas the Li-In electrode acted as the counter/reference electrode, and the scan rate was 5 mV s^{-1}. The DCIR was measured using the following procedure: the cell was first rested for 6 h and charged to 4.0 V at 0.2C under the constant current-constant voltage condition, and then rest-charge-rest-discharge was repeated with 20 min of rest and 10 s of galvanostatic charge and discharge. The C-rate was 0.025, 0.05, 0.1, 0.2, 0.3, 0.5, or 1.0C. Glove box (MSIT-24-0100) at Institute for Battery Research Innovation (RS-2023-00261543) was used. A pressure sensor with a resolution of 0.1 kg (load cell, BONGSHIN) was used in OEP, and the operating pressure was set to 3 MPa instead of 0.3 MPa due to the resolution limitations of the load cell.

Supporting Information

Supporting Information is available from the Wiley Online Library or from the author.

Acknowledgements

This work was supported by LG Energy Solution, by the National Research Foundation of Korea (NRF) grant funded by the Korea government (MSIT) (No. RS-2024-00343349 and RS-2025-25441254).

Conflict of Interest

The authors declare no conflict of interest.

Data Availability Statement

The data that support the findings of this study are available from the corresponding author upon reasonable request.

Keywords

in situ cross-linking binders, low-pressure operation, solid-state batteries, sulfide solid electrolytes, thiol-ene click reaction

Received: June 23, 2025
Revised: September 13, 2025
Published online: January 28, 2026

[1] D. Larcher, J. M. Tarascon, *Nat. Chem.* **2015**, *7*, 19.
[2] J. Janek, W. G. Zeier, *Nat. Energy* **2016**, *1*, 16141.
[3] Y. Kato, S. Hori, T. Saito, K. Suzuki, M. Hirayama, A. Mitsui, M. Yonemura, H. Iba, R. Kanno, *Nat. Energy* **2016**, *1*, 16030.
[4] A. Manthiram, X. Yu, S. Wang, *Nat. Rev. Mater.* **2017**, *2*, 16103.
[5] M. Li, J. Lu, Z. Chen, K. Amine, *Adv. Mater.* **2018**, *30*, 1800561.
[6] J. Wang, Y. Yamada, K. Sodeyama, E. Watanabe, K. Takada, Y. Tateyama, A. Yamada, *Nat. Energy* **2018**, *3*, 22.
[7] J. Schnell, T. Günther, T. Knoche, C. Vieider, L. Köhler, A. Just, M. Keller, S. Passerini, G. Reinhart, *J. Power Sources* **2018**, *382*, 160.
[8] T. Krauskopf, F. H. Richter, W. G. Zeier, J. Janek, *Chem. Rev.* **2020**, *120*, 7745.
[9] Q. Zhao, S. Stalin, C.-Z. Zhao, L. A. Archer, *Nat. Rev. Mater.* **2020**, *5*, 229.
[10] M. J. Wang, E. Kazyak, N. P. Dasgupta, J. Sakamoto, *Joule* **2021**, *5*, 1371.
[11] S. Puls, E. Nazmutdinova, F. Kalyk, H. M. Woolley, J. F. Thomsen, Z. Cheng, A. Fauchier-Magnan, A. Gautam, M. Gockeln, S.-Y. Ham, M. T. Hasan, M.-G. Jeong, D. Hiraoka, J. S. Kim, T. Kutsch, B. Lelotte, P. Minnmann, V. Miß, K. Motohashi, D. L. Nelson, F. Ooms, F. Piccolo, C. Plank, M. Rosner, S. E. Sandoval, E. Schlautmann, R. Schuster, D. Spencer-Jolly, Y. Sun, B. S. Vishnugopi, et al., *Nat. Energy* **2024**, *9*, 1310.
[12] K. Zhou, S. Lu, C. Mish, Y.-T. Chen, S. Feng, J. Kim, M.-S. Song, H. A. Kim, P. Liu, *ACS Energy Lett.* **2025**, *10*, 966.
[13] J. Janek, W. G. Zeier, *Nat. Energy* **2023**, *8*, 230.
[14] A. Sakuda, A. Hayashi, M. Tatsumisago, *Sci. Rep.* **2013**, *3*, 2261.
[15] K. H. Park, Q. Bai, D. H. Kim, D. Y. Oh, Y. Zhu, Y. Mo, Y. S. Jung, *Adv. Energy Mater.* **2018**, *8*, 1800035.
[16] Y.-G. Lee, S. Fujiki, C. Jung, N. Suzuki, N. Yashiro, R. Omoda, D.-S. Ko, T. Shiratsuchi, T. Sugimoto, S. Ryu, J. H. Ku, T. Watanabe, Y. Park, Y. Aihara, D. Im, I. T. Han, *Nat. Energy* **2020**, *5*, 299.
[17] Y. B. Song, K. H. Baeck, H. Kwak, H. Lim, Y. S. Jung, *Adv. Energy Mater.* **2023**, *13*, 2301142.
[18] M. Liu, E. Lu, S. Wang, S. Feng, J. Gao, W. Yan, J. W. Oh, M.-S. Song, J. Luo, P. Liu, *ACS Energy Lett.* **2025**, *10*, 1389.
[19] P. Minnmann, J. Schubert, S. Kremer, R. Rekers, S. Burkhardt, R. Ruess, A. Bielefeld, F. H. Richter, J. Janek, *J. Electrochem. Soc.* **2024**, *171*, 060514.
[20] M. Yamamoto, Y. Terauchi, A. Sakuda, M. Takahashi, *Sci. Rep.* **2018**, *8*, 1212.
[21] D. Y. Oh, Y. J. Nam, K. H. Park, S. H. Jung, S.-J. Cho, Y. K. Kim, Y.-G. Lee, S.-Y. Lee, Y. S. Jung, *Adv. Energy Mater.* **2015**, *5*, 1500865.
[22] F. Hippauf, B. Schumm, S. Doerfler, H. Althues, S. Fujiki, T. Shiratsuchi, T. Tsujimura, Y. Aihara, S. Kaskel, *Energy Stor. Mater.* **2019**, *21*, 390.
[23] D. Y. Oh, Y. J. Nam, K. H. Park, S. H. Jung, K. T. Kim, A. R. Ha, Y. S. Jung, *Adv. Energy Mater.* **2019**, *9*, 1802927.
[24] K. T. Kim, D. Y. Oh, S. Jun, Y. B. Song, T. Y. Kwon, Y. Han, Y. S. Jung, *Adv. Energy Mater.* **2021**, *11*, 2003766.
[25] K. T. Kim, T. Y. Kwon, Y. S. Jung, *Curr. Opin. Electrochem.* **2022**, *34*, 101026.
[26] K. Lee, J. Lee, S. Choi, K. Char, J. W. Choi, *ACS Energy Lett.* **2019**, *4*, 94.
[27] R. Li, N. Chen, S. Liu, Y. Mao, Z. Liao, K. Qiu, P. Wang, T. Zhang, S. Hao, G. Zhu, C. Guo, X. Liu, D. Ren, L. Lu, M. Ouyang, *Adv. Funct. Mater.* **2024**, *34*, 2409403.
[28] T. Y. Kwon, K. T. Kim, D. Y. Oh, Y. B. Song, S. Jun, Y. S. Jung, *Energy Stor. Mater.* **2022**, *49*, 219.
[29] R. Koerver, W. Zhang, L. de Biasi, S. Schweidler, A. O. Kondrakov, S. Kolling, T. Brezesinski, P. Hartmann, W. G. Zeier, J. Janek, *Angew. Chem., Int. Ed.* **2018**, *11*, 2142.
[30] J. Woo, Y. B. Song, H. Kwak, S. Jun, B. Y. Jang, J. Park, K. T. Kim, C. Park, C. Lee, K. H. Park, H. W. Lee, Y. S. Jung, *Adv. Energy Mater.* **2023**, *13*, 2203292.
[31] S. Kalnaus, N. J. Dudney, A. S. Westover, E. Herbert, S. Hackney, *Science* **2023**, *381*, 1300.
[32] X. Gao, B. Liu, B. Hu, Z. Ning, D. S. Jolly, S. Zhang, J. Perera, J. Bu, J. Liu, C. Doerrer, E. Darnbrough, D. Armstrong, P. S. Grant, P. G. Bruce, *Joule* **2022**, *6*, 636.
[33] J. T. Kim, H.-J. Shin, A. Y. Kim, H. Oh, H. Kim, S. Yu, H. Kim, K. Y. Chung, J. Kim, Y.-K. Sun, H.-G. Jung, *J. Mater. Chem. A* **2023**, *11*, 20549.
[34] Y. Zhao, Z. Qiang, Y. Ning, D. Li, T. Jiang, S. Lou, *Nano Energy* **2024**, *131*, 110295.
[35] X. Jiao, J. Yin, X. Xu, J. Wang, Y. Liu, S. Xiong, Q. Zhang, J. Song, *Adv. Funct. Mater.* **2021**, *31*, 2005699.
[36] L. Hu, X. Zhang, P. Zhao, H. Fan, Z. Zhang, J. Deng, G. Ungar, J. Song, *Adv. Mater.* **2021**, *33*, 2104416.
[37] G. Yu, G. Ye, C. Wang, C. Wang, Z. Wang, P. Hu, Y. Li, X.-X. Feng, S.-J. Tan, M. Yan, S. Xin, Z. Liu, *Sci. China: Chem.* **2024**, *67*, 1028.
[38] J. Zhang, Y. Zhai, Z. Zhao, J. He, W. Wei, J. Xiao, S. Wu, Q.-H. Yang, *Acta. Phys. Chim. Sin.* **2024**, *40*, 2306006.
[39] Z.-Y. Gu, J.-M. Cao, J.-Z. Guo, X.-T. Wang, X.-X. Zhao, S.-H. Zheng, Z.-H. Sun, J.-L. Yang, K.-Y. Zhang, H.-J. Liang, K. Li, X.-L. Wu, *J. Am. Chem. Soc.* **2024**, *146*, 4652.
[40] C. Mao, J. Dong, J. Li, X. Zhai, J. Ma, S. Luan, X. Shen, Y. Wang, P. Zhang, H. Sun, X. Bie, X. Gao, J. Song, *Adv. Mater.* **2025**, *37*, 2500079.
[41] J. S. Silverstein, B. J. Casey, M. E. Natoli, B. J. Dair, P. Kofinas, *Macromol.* **2012**, *45*, 3161.
[42] C. E. Hoyle, C. N. Bowman, *Angew. Chem., Int. Ed.* **2010**, *49*, 1540.
[43] P. Tingaut, R. Hauert, T. Zimmermann, *J. Mater. Chem.* **2011**, *21*, 16066.
[44] Y. J. Nam, D. Y. Oh, S. H. Jung, Y. S. Jung, *J. Power Sources* **2018**, *375*, 93.
[45] B. Jang, Y. B. Song, K. H. Baeck, J. Lee, S.-J. Jung, S. Choi, H.-W. Lee, Y. S. Jung, *Adv. Energy Mater.* **2025**, 02981.
[46] Y.-G. Cho, C. Hwang, D. S. Cheong, Y.-S. Kim, H.-K. Song, *Adv. Mater.* **2019**, *31*, 1804909.
[47] M. T. Ramesan, R. Alex, *Polym. Int.* **2001**, *50*, 1298.

[48] C. Decker, T. N. T. Viet, *Macromol. Chem. Phys.* **1999**, *200*, 1965.
[49] D. Wang, J. Guo, H. Zhang, B. Cheng, H. Shen, N. Zhao, J. Xu, *J. Mater. Chem. A* **2015**, *3*, 12864.
[50] M. Liu, D. Zhou, Y.-B. He, Y. Fu, X. Qin, C. Miao, H. Du, B. Li, Q.-H. Yang, Z. Lin, T. S. Zhao, F. Kang, *Nano Energy* **2016**, *22*, 278.
[51] C. Bak, K.-G. Kim, H. Lee, S. Byun, M. Lim, H. An, Y. Roh, J. Lim, C. B. Dzakpasu, D. Kim, J. Lee, H. Lee, H. Lee, Y. M. Lee, *Chem. Eng. J.* **2024**, *483*, 148913.
[52] J. H. Chang, M. W. Pin, I. Kim, S. Kim, S. Kim, S. Moon, J. Cho, S. Choi, B. Heo, Z. A. Chandio, Y. Kim, J. Y. Cheong, D. Zide, M. Madondo, B. J. Bladergroen, M. Eldessouki, M. M. Escandell, H.-J. Jeon, *J. Energy Storage* **2024**, *83*, 110729.
[53] J. Choi, J. Y. Kim, S. H. Kang, D. O. Shin, M. J. Lee, Y.-G. Lee, *J. Mater. Chem.* **2024**, *12*, 6426.
[54] P. J. Flory, *J. Chem. Phys.* **1950**, *18*, 108.
[55] Y. Kashihara, S. Okada, Y. Urahama, S. Hikasa, S. Makuta, K. Fujiwara, S. Fujii, Y. Nakamura, *J. Appl. Polym. Sci.* **2019**, *136*, 47272.
[56] C. Li, A. Strachan, *J. Polym. Sci. B: Polym. Phys.* **2015**, *53*, 103.
[57] Y. Han, S. H. Jung, H. Kwak, S. Jun, H. H. Kwak, J. H. Lee, S.-T. Hong, Y. S. Jung, *Adv. Energy Mater.* **2021**, *11*, 2100126.
[58] W. Zhang, D. A. Weber, H. Weigand, T. Arlt, I. Manke, D. Schröder, R. Koerver, T. Leichtweiss, P. Hartmann, W. G. Zeier, J. Janek, *ACS Appl. Mater. Interfaces* **2017**, *9*, 17835.
[59] S. Jun, Y. J. Nam, H. Kwak, K. T. Kim, D. Y. Oh, Y. S. Jung, *Adv. Funct. Mater.* **2020**, *30*, 2002535.
[60] W. Zhao, Y. Zhang, N. Sun, Q. Liu, H. An, Y. Song, B. Deng, J. Wang, G. Yin, F. Kong, S. Lou, J. Wang, *ACS Energy Lett.* **2023**, *8*, 5050.
[61] X.-H. Meng, X.-D. Zhang, H. Sheng, M. Fan, T. Lin, D. Xiao, J. Tian, R. Wen, W.-Z. Liu, J.-L. Shi, L.-J. Wan, Y.-G. Guo, *Angew. Chem., Int. Ed.* **2023**, *62*, 202302170.
[62] L. Ni, H. Chen, S. Guo, A. Dai, J. Gao, L. Yu, Y. Mei, H. Wang, Z. Long, J. Wen, W. Deng, G. Zou, H. Hou, T. Liu, K. Amine, X. Ji, *Adv. Funct. Mater.* **2023**, *33*, 2307126.
[63] S. H. Jung, U.-H. Kim, J.-H. Kim, S. Jun, C. S. Yoon, Y. S. Jung, Y.-K. Sun, *Adv. Energy Mater.* **2020**, *10*, 1903360.
[64] J. S. Kim, S. Jung, H. Kwak, Y. Han, S. Kim, J. Lim, Y. M. Lee, Y. S. Jung, *Energy Stor. Mater.* **2023**, *55*, 193.
[65] S. Nam, Y. Kim, S. H. Kim, H. B. Son, D.-Y. Han, Y. H. Kim, J. H. Cho, J. Park, S. Park, *ACS Appl. Mater. Interfaces* **2024**, *16*, 594.